Fiber Bragg Grating Total Temperature Probes for High-Speed Airflow With High Recovery Factor

Guoqing Han, Jianping Hu, Xianming Liu, Xiaohua Lei, and Peng Zhang

***Abstract*—The fiber Bragg grating (FBG) temperature measurement technology has advantages, such as high accuracy, small size, anti-interference, and stable performance compared to traditional thermocouple technology in high-speed airflow total temperature testing. However, low recovery factors of FBG total temperature probes at low Mach numbers have been reported, which is very detrimental to improving the accuracy of the total temperature measurement. In this article, a 3-D structure model of FBG total temperature probe is established based on the characteristics of fiber as the temperature sensing element. The temperature distribution under different probe structural parameters, such as the inner diameter of the shield, the position, and length of FBG, is analyzed using conjugate heat transfer (CHT) multiphysics field model. Combined with coupled-mode theory, the spectral characteristics of different FBG parameters and their effects on the recovery factor are analyzed. The structure of FBG total temperature probe with high recovery factor is designed. The comparative experimental results of high-speed airflow show that the improved FBG total temperature probe has a recovery factor exceeding 0.92 from Mach number 0.3–0.8 and up to 0.99 at Mach number greater than 0.4, which has even exceeded the level of most traditional thermocouple total temperature probes.**

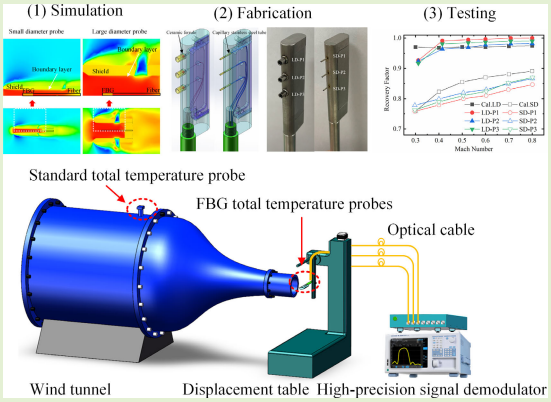

***Index Terms*—Conjugate heat transfer (CHT), coupled-mode theory, fiber Bragg grating (FBG), recovery factor, total temperature.**

I. Introduction

THE measurement of airflow temperature is a crucial aspect of evaluating, diagnosing, and predicting the operating performance and condition of aircraft engines, and it holds significant importance for the design, development, testing, production, and maintenance of aircraft engines [1], [2], [3]. The high-speed air flow temperature in aerodynamics refers to the total temperature, that is, the temperature of the air flow in the state of adiabatic stagnation. It is composed of static temperature and dynamic temperature. Static temperature represents the kinetic energy of gas molecules' free motion, while dynamic temperature represents the kinetic energy of gas molecules' directional motion. In practice, the probe cannot completely stagnate the airflow under adiabatic conditions. The recovery factor is often introduced to characterize the extent to which the total temperature probe converts the kinetic energy of the airflow into heat. The higher the recovery factor, the smaller the sum of velocity error, conduction error, and radiation under the given flow environment, and the higher the temperature measurement accuracy of the probe. In low-temperature environments where the airflow temperature is less than 300 °C, the recovery factor of conventional thermocouple total temperature probes ranges from 0.90 to 0.98 [4], [5].

Due to the electrical circuit structure and insulation treatment of thermocouples, the probe fabrication is complex and the size is large. This is especially noticeable for multipoint

Manuscript received 14 September 2023; accepted 3 October 2023. Date of publication 13 October 2023; date of current version 14 November 2023. This work was supported in part by the National Natural Science Foundation of China under Grant 61875023, Grant 51975077, and Grant 52175530. The associate editor coordinating the review of this article and approving it for publication was Prof. Arnaldo G. Leal-Junior. *(Corresponding author: Xianming Liu.)*

Guoqing Han, Xianming Liu, Xiaohua Lei, and Peng Zhang are with the Key Laboratory of Optoelectronic Technology and Systems Ministry of Education, College of Optoelectronic Engineering, Chongqing University, Chongqing 400044, China (e-mail: guoqinghan18@163.com; xianming65@163.com; xhlei@cqu.edu.cn; zhangpeng@cqu.edu.cn).

Jianping Hu is with the School of Power and Energy, Northwestern Polytechnical University, Xi'an, Shaanxi 710072, China (e-mail: hujp@nwpu.edu.cn).

Digital Object Identifier 10.1109/JSEN.2023.3322713

total temperature probes [6]. In addition, electromagnetic interference, freezing point error, and channel error make it extremely difficult to improve the temperature measurement accuracy of thermocouple total temperature probes. With the development of fiber optic sensing technology, fiber optic temperature measurement technologies, such as fiber Bragg grating (FBG), have been used for high-speed airflow total temperature testing due to their small size, high sensitivity, stable performance, and easy multiplexing [7], [8], [9], [10], [11]. Polz et al. [12] conducted research on FBG total temperature probes for testing inlet airflow of compressors. Five FBG-based total temperature probes and one thermocouple-based total temperature probe were installed on compressor blades for wind tunnel testing [13]. At Mach numbers ranging from 0.3 to 0.8, the FBG total temperature probes showed good mechanical robustness, proving that using FBG as the temperature sensing element for measuring high-speed airflow total temperature is feasible, and can effectively reduce the size of the probe compared to thermocouple probes. However, the recovery factor based on the FBG total temperature probe ranged from 0.79 to 0.99, and the recovery factor was generally less than 0.9 at Mach numbers below 0.6. Compared with traditional thermocouple-based total temperature probes, the recovery factor was significantly lower, and there was an obvious difference in the recovery factor of probes with the same structure. Currently, there are no research reports on the analysis and improvement of the recovery factor of FBG total temperature probes.

In this article, a conjugate heat transfer (CHT) multiphysics field model is established for the FBG total temperature probe based on its temperature sensing characteristics, and the temperature field distribution is analyzed under different parameters, such as probe structural dimension, FBG position, and FBG length. Furthermore, combining coupled-mode theory, the spectral influence of FBG at different grating lengths on temperature measurement performance is analyzed. Combining CHT and FBG spectral theory analysis, an optimized FBG total temperature probe structure is obtained. The recovery factor of the optimized FBG total temperature probe was tested through high-speed wind tunnel experiments to verify its performance.

II. Theory

A. Total Temperature Measurement

The total temperature T_t of the airflow can be expressed as the sum of static temperature T_s and dynamic temperature T_v

$$T_{\mathrm{t}} = T_s + T_{\mathrm{v}} = T_s + \frac{v^2}{2c_p} \tag{1}$$

where v is the airflow velocity and c_p is the constant pressure specific heat capacity of airflow.

According to the equation of state for isentropic compressible flow, the relationship between total temperature and static temperature can be expressed as

$$T_t = \left(1 + \frac{\gamma - 1}{2} Ma^2\right) T_s \tag{2}$$

where Ma is the Mach number of the airflow, γ is the specific heat ratio (adiabatic coefficient) of gas, and when gas is air, γ is 1.4.

To characterize the degree to which the total temperature probe restores airflow energy to thermal energy, the recovery factor is introduced, which is defined as

$$r = \frac{T_{\mathrm{m}} - T_s}{T_{\mathrm{t}} - T_s} \tag{3}$$

where T_m represents the measured temperature of the probe. The units for T_t, T_s, and T_m are all in Kelvin (K) when calculating the recovery factor. Combined with (2), the experimental determination formula for the recovery factor can be deduced as

$$r = 1 - \frac{T_t - T_m}{T_t}\left[1 + \frac{2}{(\gamma - 1)Ma^2}\right]. \tag{4}$$

The recovery factor of the probe was determined in a standard wind tunnel, which provides the total temperature and Mach number of the freestream flow. Based on the measured temperature at this point, the recovery factor can be obtained.

When the total temperature of the freestream flow is below 300 °C, conduction and radiation errors can be ignored due to the high length–diameter ratio of the optical fiber (greater than 20) and its relatively low thermal conductivity [1.47 W/(m·K)]. The relationship between velocity error and recovery factor is

$$\Delta T_v = (1 - r)\left[\frac{\frac{(\gamma-1)Ma^2}{2}}{1 + \frac{(\gamma-1)Ma^2}{2}}\right] T_t. \tag{5}$$

When the total temperature and Mach number of the incoming flow are determined, a larger recovery factor will result in smaller velocity error and total temperature measurement error.

B. FBG and Spectral Characteristics

FBG is a passive device formed by periodically modulating the refractive index of the optical fiber core through a certain method to form a diffraction grating. Essentially, it is a narrowband filter in the fiber core. When a broadband light passes through FBG, the light that satisfies the Bragg wavelength condition of FBG will be reflected, and the light of other wavelengths will continue to transmit through FBG. The Bragg wavelength (resonant wavelength of the reflection spectrum) λ_B of FBG is determined by the grating period Λ and the effective refractive index n_{eff} of the fiber core

$$\lambda_B = 2n_{\mathrm{eff}}\Lambda. \tag{6}$$

The changes in the external temperature will result in changes in the effective refractive index n_{eff} and the grating period Λ of FBG. The Bragg wavelength λ_B of the reflection spectrum is a function of temperature. The ambient temperature can be obtained by measuring λ_B and calculated with

$$T = \frac{1}{K_T}\left(\lambda_B - \lambda_{T_0}\right) + T_0 \tag{7}$$

where λ_{T0} is the Bragg wavelength at temperature T_0, and K_T is the temperature sensitivity coefficient of the fiber grating,

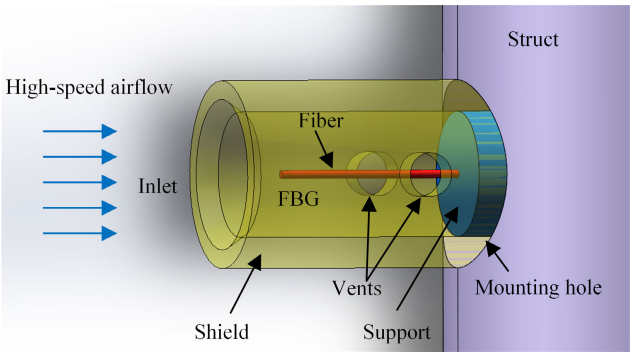

Fig. 1. Structure of FBG total temperature probe.

mainly determined by the thermal-optic coefficient and thermal expansion coefficient of the fiber grating.

The reflection spectrum of an FBG with length L can be expressed with coupled-mode theory [14] as

$$R(\lambda) = \frac{\kappa\kappa^* \sinh^2(sL)}{s^2\cosh^2(sL) + \hat{\sigma}^2 \sinh^2(sL)} \tag{8}$$

where κ and κ^* are the ac coupling coefficients and $\hat{\sigma}$ is the dc coupling coefficient. The specific expression is as follows:

$$\begin{cases} \kappa = \kappa^* = \dfrac{\pi}{\lambda}\Delta n_{\text{eff}} \\ s^2 = \kappa^2 - \hat{\sigma}^2 \\ \hat{\sigma} = \delta + \kappa_{11} \\ \delta = \beta - \dfrac{\pi}{\Lambda} \\ \kappa_{11} = \dfrac{2\pi}{\lambda}\Delta n_{\text{eff}} \end{cases} \tag{9}$$

where Δn_{eff} is the average change in effective refractive index, δ is the detuning, κ_{11} represents the self-coupling coefficient of the mode, and β is the propagation constant.

III. Simulation Analysis

The basic structure of the total temperature probe with FBG as a temperature sensing element is shown in Fig. 1. The design adopts a longitudinal shield, where the fiber, shield, support, and mounting hole of struct are all centered. Two vents are symmetrically distributed along the circumferential direction on the shield. These vents regulate the airflow velocity within the FBG temperature measurement area and thus adjust the temperature distribution. The FBG is located at the end of the fiber and parallel to the far-field freestream flow direction. This structure is essentially similar to that of a traditional thermocouple probe, with the main difference being that the temperature sensing element in the FBG probe is a single-ended fiber, whereas it is a thermocouple junction created and supported by two different material wires in the thermocouple probe.

A. Probe Modeling

According to the basic structure of the total temperature probe shown in Fig. 1, a finite element numerical analysis method based on CHT is used for flow field modeling and simulation. In the FBG total temperature probe with a shield,

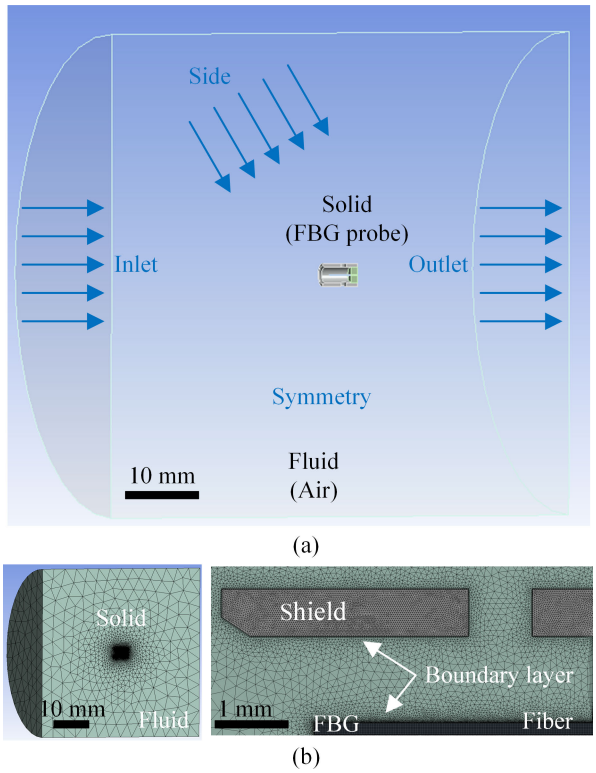

Fig. 2. Simulation diagram. (a) Boundary conditions. (b) Computational domain.

TABLE I
Property Parameters of Materials in the Calculation Domain

Calculation domain	Material	Density, Kg/m^3	Specific heat capacity, J/(Kg·K)	Thermal conductivity, W/(m·K)
air	air	ideal-gas	1006.43	0.0242
fiber	silica	2200	772	1.47
shield/ support	stainless steel	8030	502.48	16.27

the boundary layer has a significant impact on heat transfer computation. Therefore, the shear stress transfer (SST) k-ω turbulence model for internal flow is adopted to accurately analyze boundary layer characteristics [15]. The detailed information of multiphysics fields near the wall is obtained by enhanced wall treatment.

Due to the symmetry of the simulation model, only half of the simulation model was considered to reduce computational cost. The inlet boundary (including inlet and side) was set as a given pressure far field with specified Mach number and static temperature to simulate free compressible flow at infinity, while the outlet boundary was set as a given pressure outlet with specified backflow total temperature. The computational domain is shown in Fig. 2.

The computational domain consists of air as the fluid and solid components, including optical fiber, support, and shield. The optical fiber is made of silica, whereas the support tube and shield are made of stainless steel, with their respective material properties shown in Table I. In order to improve the

TABLE II
SIMULATION PARAMETERS FOR TWO DIFFERENT INNER DIAMETERS OF SHIELD

Symbol	Quantity	Small diameter probes	Large diameter probes
D_{shield_out}	outer diameter of shield	0.8	3
D_{shield_in}	inner diameter of shield	0.55	2
D_{vent}	diameter of vent	0.20	0.75
N	amounts of vent	2	2
Ratio	area ratio of inlet and outlet	3.78	3.55
L_{end_mp}	distance from shield end face to measuring point	1	1
L_{vent}	distance from shield end face to vent	3	3
L_{shield}	distance from shield end face to struct	4	4
$R_{l\text{-}d}$	length-diameter ratio	24	24

accuracy of the heat transfer computation, a coupled mesh was used for the contact surfaces of the fluid and solid components. An unstructured mesh was adopted for the fluid, whereas structured meshes were used for solid components, such as the shield and optical fiber, with local refinement applied.

Previous research has utilized smaller shield designs to reduce the size of the probe head, but as optical fiber element has a large length–diameter ratio, it is difficult to ensure complete centering when integrating them into the probe. Even if the root of fiber is centered, slight tilt angle can cause the temperature sensing grating to deviate from the shield axis and adhere to its interior surface when the shield inner diameter is too small. In addition, in high-speed airflow impact, the optical fiber may tilt and adhere to the wall. There are three factors to consider when choosing the right probe diameter. First, the overall measurement error needs to be minimal. Second, the interference between the probe and the flow field should be reduced as much as possible. Finally, it is also necessary to fully consider the strength and manufacturing difficulty of the shield material. Taking these factors into account, a probe diameter range of 0.55-mm minimum and 2-mm maximum is a viable option. According to [5], the area ratio of inlet and outlet is usually maintained between 3 and 4 with an internal Mach number of 0.1–0.15 to achieve the minimum of total error, mainly velocity error for low-temperature applications. Additionally, in order to minimize interference with the flow field being measured, the internal diameter of the shield (D_{shield_in}) is generally not greater than 2 mm. Considering the existing strength and processing difficulty of capillary stainless steel tubes, the diameter of the shield can be as small as 0.55 mm for tiny FBG. Typically, there are two vent holes symmetrically arranged; therefore, the diameter of the vent hole (D_{vent}) is also determined. Simulation modeling and analysis were carried out using the same parameters as those used in the experiment, as shown in Table II. The dimensions of the shield of the probe are shown in Fig. 3.

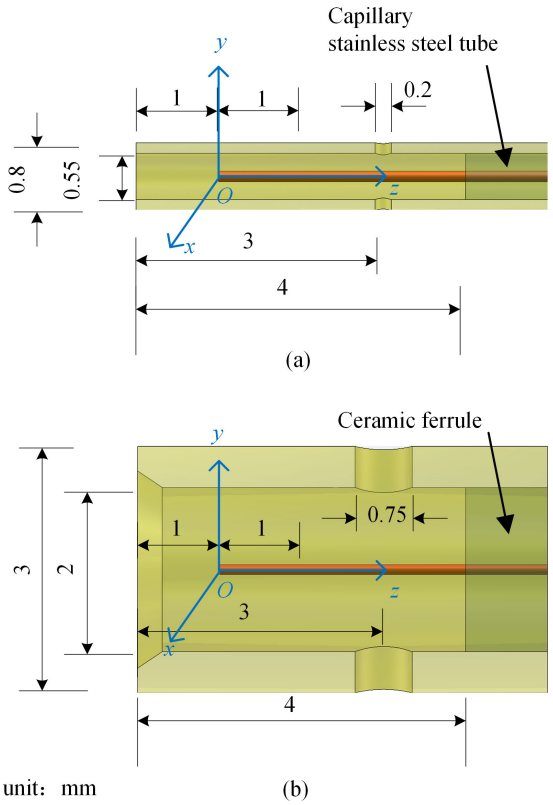

Fig. 3. Schematic of simulation structural parameters. (a) Small diameter probe. (b) Large diameter probe.

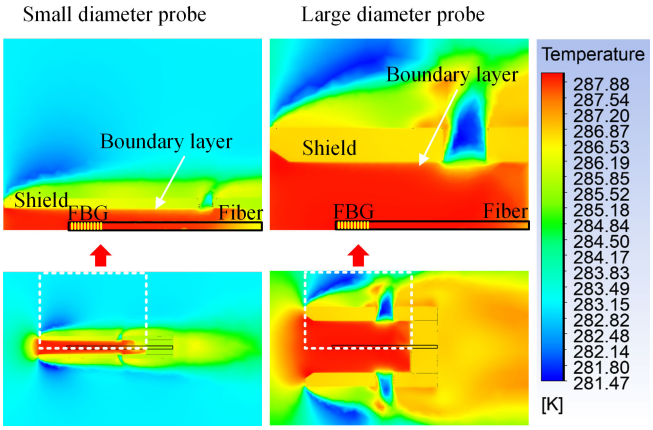

Fig. 4. Temperature contours of small and large diameter probes.

B. CHT Model

The inlet airflow total temperature was set to 288.15 K (15 °C), with Mach numbers ranging from 0.3 to 0.8. The temperature contour near the shield of the two probes with different sizes at $Ma = 0.8$ is shown in Fig. 4. A portion of the airflow is stopped at the shield inlet, while another portion is stopped at the tip of the fiber. The two stagnations allow the total temperature probe to achieve a high recovery factor. For probes with small inner diameters, the corresponding thermal boundary layer accounts for a larger proportion along the radial direction, which makes the surface temperature of the optical fiber vulnerable to low-temperature airflow near the wall and may result in lower recovery factor.

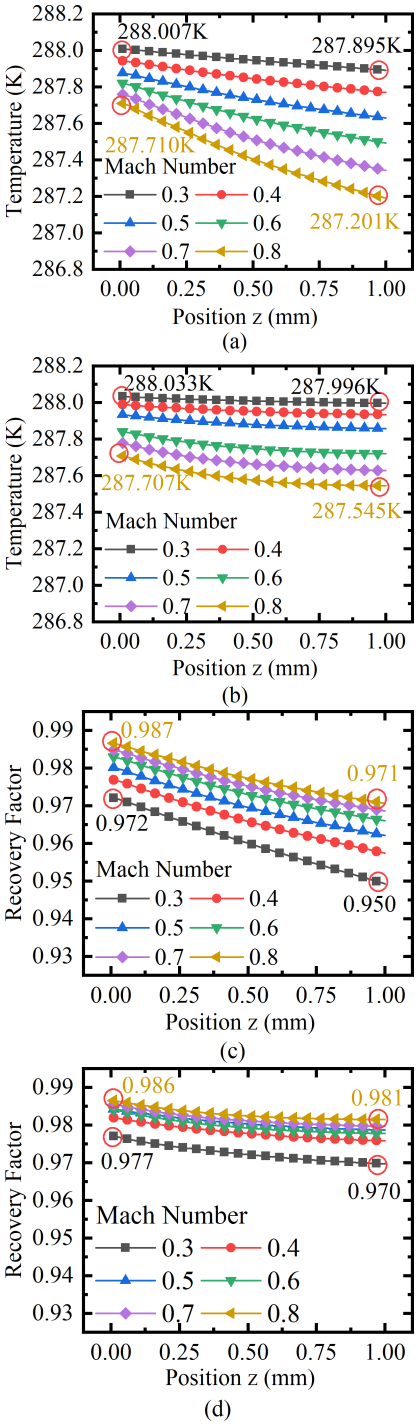

Fig. 5. Temperature distribution in FBG (length = 1 mm) at different Mach numbers for (a) small diameter probes and (b) large diameter probes. Recovery factors in FBG (length = 1 mm) at different Mach numbers for (c) small diameter probes and (d) large diameter probes.

Assuming that the fiber is not bent and absolutely centered, the temperature distribution within 1 mm of the fiber axis in two different probe sizes at different Mach numbers is simulated, as shown in Fig. 5. The corresponding recovery factor is also calculated. It can be found that the closer to the fiber end, the higher the temperature. The larger the Mach number, the lower the temperature, and the greater the temperature difference between the end and 1 mm position.

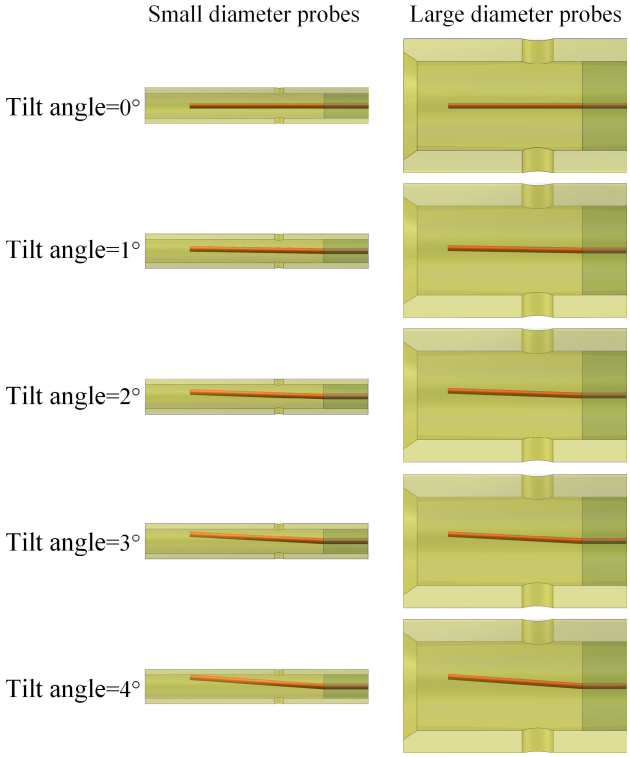

Fig. 6. Schematic of different tilt angles.

Compared to large diameter probes, small diameter probes have a larger temperature difference, reaching 0.5 K at Mach number of 0.8. Therefore, the position of FBG on the optical fiber has a great influence on the temperature measurement results.

To investigate the effect of tilt angle on the recovery factor of the probe, simulation models were established with tilt angles set at 0°–4°, as shown in Fig. 6. The temperature at 0.5 mm from the end of the fiber (the center position of the grating) is taken as the FBG temperature, and the recovery factors at different tilt angles and different Mach numbers are calculated, as shown in Fig. 7. As the tilt angle gradually increases from 0° to 4°, the recovery factor of the small diameter probe decreases gradually, reaching a minimum of only about 0.75. When the tilt angle is 4°, the recovery factor increases from 0.75 to 0.90 as the Mach number increases from 0.3 to 0.8, while the recovery factor of the large diameter probe remains around 0.97 at different tilt angles and Mach numbers, showing good stability.

C. FBG Parameter Optimization

According to the recovery factor formula (4), the relationship between the recovery factor and the position and length of the FBG is shown in Fig. 8. The closer the FBG element to the fiber end and the shorter its length, the higher the recovery factor. According to the principle of FBG temperature sensing, the temperature at the midpoint of the FBG is taken as the measured temperature [16], and it can be observed that the shorter the length, the higher the recovery factor. Therefore, the FBG should be located at the end of the fiber and its length should be kept to a minimum. However, FBG needs to have

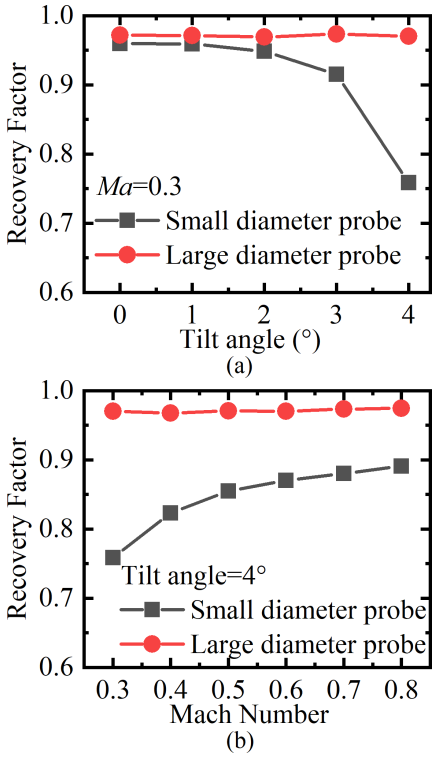

Fig. 7. Comparison of recovery factors between large and small diameter probes. (a) Different tilt angles (Ma = 0.3). (b) Different Mach numbers (tilt angle = 4°).

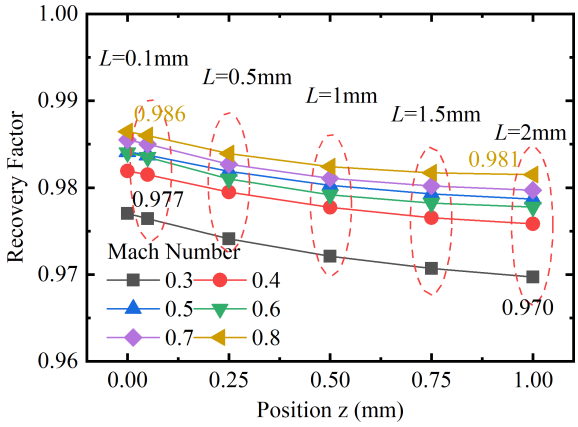

Fig. 8. Recovery factor at different positions (z = 0 refers to the end of the fiber).

good spectral quality to ensure temperature sensing accuracy, and its length cannot be too small. In order to obtain the optimal length of FBG, the temperature measurement accuracy needs to be analyzed by its spectral signal.

Based on coupled-mode theory (8), the spectra of five typical lengths of FBGs were simulated, with the simulation parameters shown in Table III. The spectra of FBGs with different lengths are shown in Fig. 9(a).

To characterize the changes in FBG spectrum characteristics, peak reflectivity and full-width at half-maximum (FWHM) were selected as two core spectral indicators. When phase matching, i.e., $\hat{\sigma}$ = 0, (10) attains its maximum value

TABLE III
SIMULATION PARAMETERS BASED ON COUPLED-MODE THEORY

Symbol	Quantity	Value
L	FBG length (mm)	0.1, 0.5, 1, 1.5, 2
n_{eff}	effective refractive index of the fiber core	1.467
Δn_{eff}	effective refractive index modulation	5×10^{-4}
Λ	grating period (nm)	528.1090
λ_{span}	spectral range (nm)	1550-1554
$\lambda_{internal}$	spectral interval (nm)	0.001

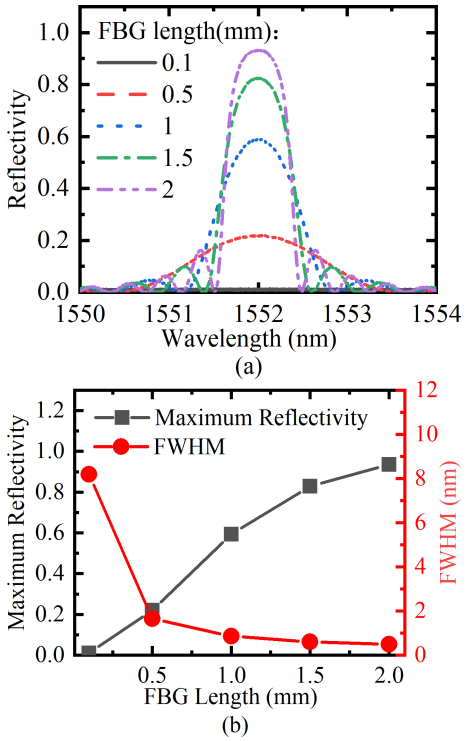

Fig. 9. (a) FBG spectra. (b) Characteristic parameters of FBG spectra.

(peak reflectivity)

$$R_{\max} = \tanh^2(\kappa L) = \tanh^2\left(\frac{\pi}{\lambda_B}\Delta n_{\text{eff}} L\right). \tag{10}$$

According to the definition of FWHM

$$R\left(\lambda_B \pm \frac{\text{FWHM}}{2}\right) = \frac{1}{2}R(\lambda_B). \tag{11}$$

The approximate value can be calculated as

$$\text{FWHM} = \lambda_B \sqrt{\left(\frac{\Delta n_{\text{eff}}}{2n_{\text{eff}}}\right)^2 + \left(\frac{\Lambda}{L}\right)^2}. \tag{12}$$

As the FBG length decreases, the spectral maximum reflectivity decreases and the FWHM expands. The peak reflectivity of the 0.1-mm FBG is only 1%, and the FWHM is as high as 8 nm, as shown in Fig. 9(b), which will cause a decrease in

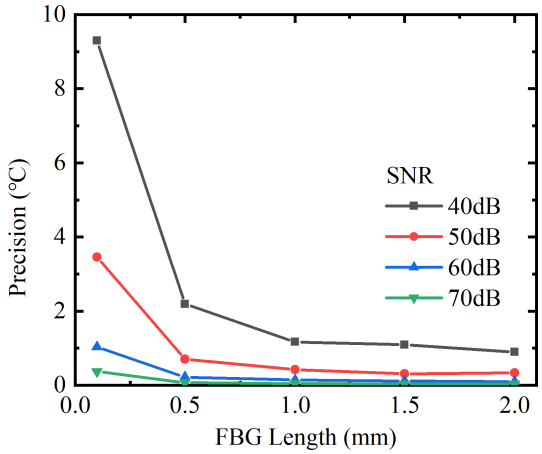

Fig. 10. Temperature demodulation accuracy at different SNRs.

temperature measurement accuracy due to the extremely low reflectivity and wide spectrum.

The temperature measurement accuracy of the above spectra is determined by adding random noise, and the signal-to-noise ratio (SNR) of the spectra after adding noise is usually in the range of 40–70 dB. When the length of the grating decreases, the temperature measurement accuracy decreases, as shown in Fig. 10. To achieve a high recovery factor while ensuring a certain level of temperature measurement accuracy, a 1-mm-long FBG was ultimately chosen as the sensing element for the total temperature probe.

IV. Experiments and Results

A. Assembly of Total Temperature Probe

The structure of the probes used in the experiment was consistent with the simulation parameters described above, as shown in Fig. 11. Two types of total temperature probes with different parameters were deployed with three measurement points spaced 10 mm apart, ensuring that all three measurement points were located in the uniform flow field area at the center of the wind tunnel exit during testing. LD-Px and SD-Px correspond to the xth point of the large and small diameter probe, respectively. Microscopic images of the vent showed that the optical fiber and shield were horizontally centered. Compared to the capillary stainless steel tube used as a support for the small diameter probe, the large diameter probe employed a standard ceramic ferrule, which can maintain precise coaxial alignment between the optical fiber and the shield. All FBGs were written using UV laser and phase mask methods, with a central wavelength of 1552 nm and a grating length of 1 mm. To reduce the adverse effects of the acrylate coating on temperature measurement, the coating was removed from the grating region.

B. Calibration Experiments and Results

The static temperature calibration test system for the total temperature probe is shown in Fig. 12. It consists of FBG measurement system, high-precision platinum resistance, and constant temperature bath. The total temperature probe was placed in a high-precision thermostatic bath

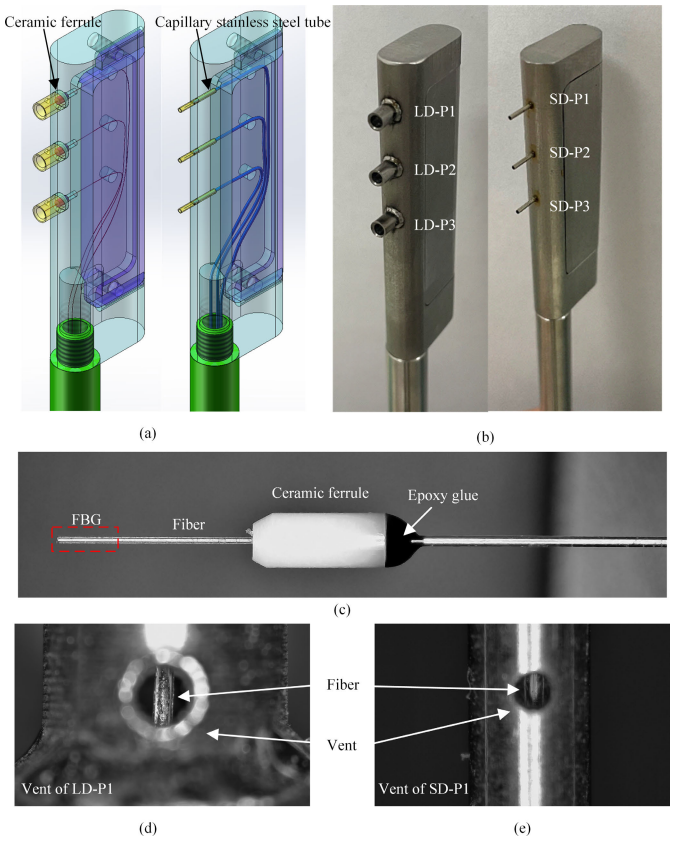

Fig. 11. Schematic of probes. (a) Three-dimensional structure diagram. (b) Picture. (c) High-accuracy positioning of large diameter probe with ceramic ferrule. (d) Microscope close-up of vent of LD-P1. (e) Microscope close-up of vent of SD-P1.

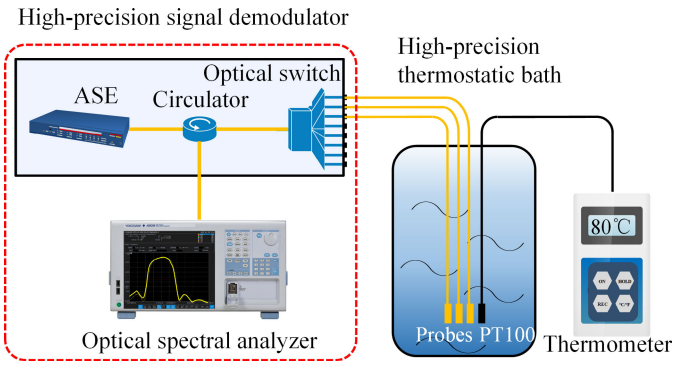

Fig. 12. Calibration experimental setup.

(TENLIN BD0515, span −5 °C–100 °C, fluctuation 0.01 °C, and uniformity 0.01 °C) for temperature testing. The spectra of the FBG were acquired using a high-precision spectrometer (YOKOGAWA AQ6380, wavelength accuracy ±5 pm). As a temperature reference, a calibrated PT100 resistance thermometer with a maximum uncertainty of $\pm(0.1 + 0.0005t)$ °C (t is the measured temperature, and the measuring instrument is OMEGA HH376 with a resolution of 0.01 °C) was used. Temperatures were cycled twice from 10 °C to 80 °C in steps of 10 °C.

The spectra at different temperatures are shown in Fig. 13(a), with the spectra gradually shifting to longer wavelengths as the temperature increases. The peak wavelength of

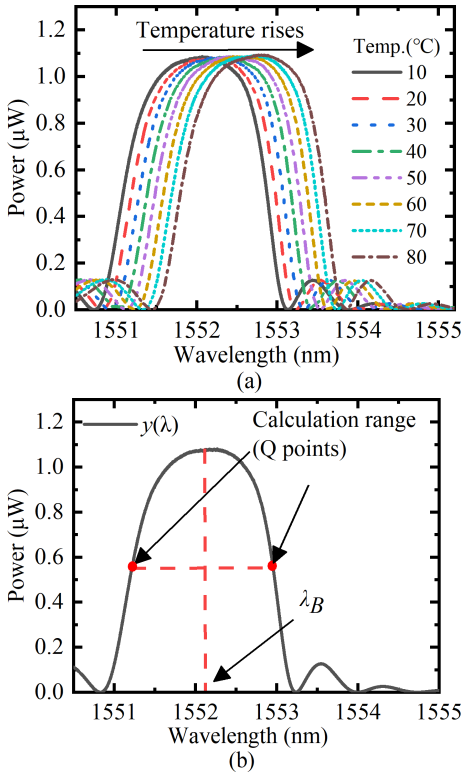

Fig. 13. (a) FBG spectra at different temperatures. (b) Schematic for solving Bragg wavelength.

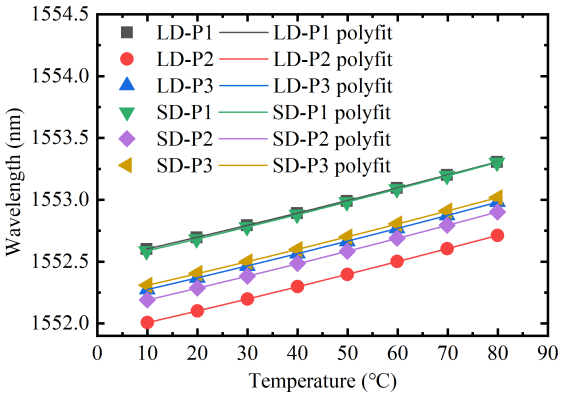

Fig. 14. Characteristic wavelengths of the FBG spectra at different temperatures.

the FBG was obtained using the centroid algorithm for all spectra. The centroid algorithm uses the geometric center of the reflection spectrum as the demodulation wavelength λ_B of the FBG, as shown in Fig. 13(b). The corresponding formula for calculating the peak wavelength λ_B is [17]

$$\lambda_B = \frac{\sum_{i=1}^{Q} y(\lambda_i) \cdot \lambda_i}{\sum_{i=1}^{Q} y(\lambda_i)} \tag{13}$$

where Q is the number of sampling points of the FBG spectrum and $y(\lambda_i)$ is the light intensity at λ_i.

At the same temperature, multiple sets of spectra were continuously acquired and the average peak wavelength was taken as the demodulated Bragg wavelength, which was then correlated with temperature, as shown in Fig. 14.

TABLE IV
TEMPERATURE-WAVELENGTH CALIBRATION COEFFICIENTS OF PROBES

Probes	λ_B(0°C), nm	A, pm/°C	B, pm/°C^2	Adj. R-Sq
LD-P1	1552.51124	9.15	1.02242×10^{-2}	0.9999
LD-P2	1551.91401	9.18	1.00532×10^{-2}	0.9999
LD-P3	1552.18227	9.16	1.05005×10^{-2}	0.9999
SD-P1	1552.49528	9.19	1.14638×10^{-2}	0.9999
SD-P2	1552.09653	9.25	1.03688×10^{-2}	0.9999
SD-P3	1552.21598	9.16	1.09481×10^{-2}	0.9999

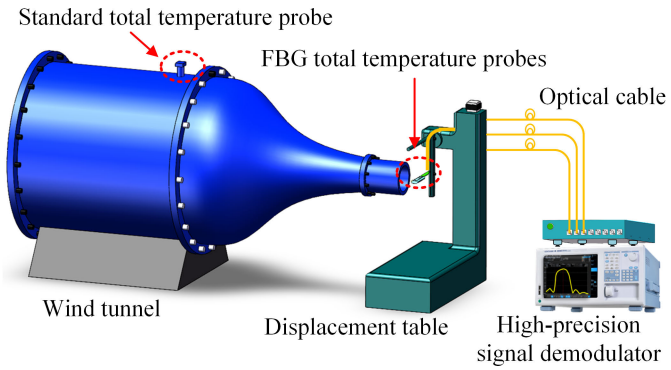

Fig. 15. High-speed airflow experimental setup.

FBG is usually fitted with a second-order polynomial function at low temperatures to achieve high-temperature measurement accuracy. Equation (14) represents the temperature-wavelength response of the probe. The corresponding coefficients are shown in Table IV. The adjusted R-squared (Adj. R-Sq) values for all total temperature probes were 0.9999, indicating that the calibration coefficients fit the temperature-wavelength characteristics of the probe very well

$$\lambda_B(T) = \lambda_B(0\ ^\circ\mathrm{C}) + A \cdot T + B \cdot T^2. \tag{14}$$

C. High-Speed Airflow Experiments and Results

The recovery factor test of the FBG total temperature probe was conducted in a high-speed wind tunnel. The exit diameter of the wind tunnel was 80 mm, and all the three FBG total temperature probes were placed in the uniform flow field area at the center of the wind tunnel exit, approximately 50 mm from the exit. The inlet of shield was facing the inlet airflow direction, as shown in Fig. 15.

First, the wind tunnel was set to a Mach number of 0.5 and left to preheat for over 30 min. Then, the Mach number increased from 0.3 to 0.8, and the test was carried out at intervals of 0.1. After the Mach number was stabilized, the total temperature inside the wind tunnel and the temperature data measured by the FBG total temperature probes were recorded, and the results are shown in Fig. 16.

Based on the data shown in Fig. 16, the recovery factors for both probes were further calculated and are shown in Fig. 17.

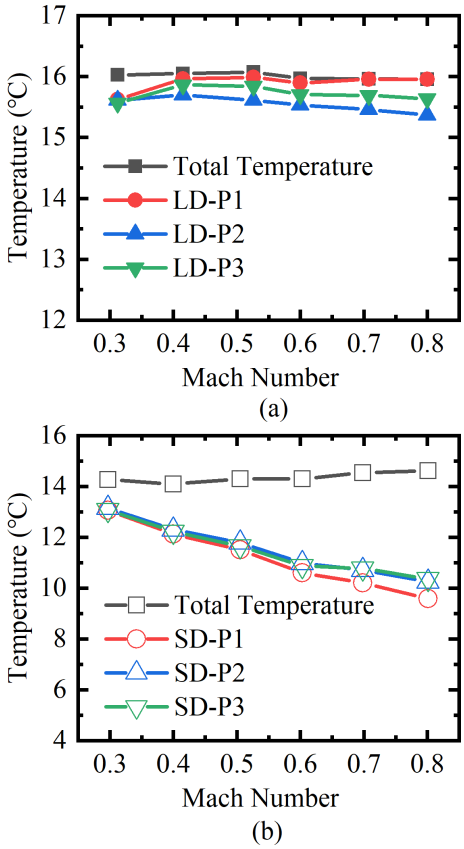

Fig. 16. Total temperature and measured temperature. (a) Large diameter probes. (b) Small diameter probes.

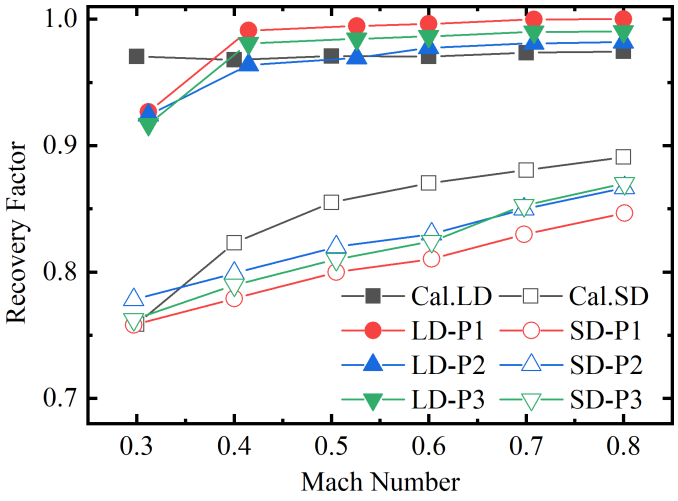

Fig. 17. Comparison of recovery factors between large diameter probes and small diameter probes, including measured and calculated recovery factors.

For the small diameter probe, the recovery factor was only between 0.76 and 0.87 at Mach numbers ranging from 0.3 to 0.8. This indicates that under the influence of high-speed airflow, the fiber may have tilted or adhered to the wall, resulting in a lower recovery factor. However, for the large diameter total temperature probe, the recovery factor was 0.92 at a Mach number of 0.3 and reached 0.99 at a Mach number of 0.4. Compared with the small diameter probe, this value has increased by over 21%.

The recovery factor of the LD-P1 sensor approaches 1 (approximately 0.99) when the Mach number exceeds 0.6. This is higher than the recovery factor of most thermocouple probes, which typically maxes out at 0.97. Such a high recovery factor may be due to two reasons. First, metals (thermocouples) have greater thermal conductivity compared to quartz (optical fiber), resulting in larger thermal conductivity errors for thermocouples, which can lead to lower measured temperatures and lower recovery factor. Second, there is a certain level of error in the temperature measurement system of the FBG itself under low freestream total temperature conditions (16 °C or 289.15 K). The errors associated with the FBG and its signal demodulation system in this study are within ±0.2 °C. According to (4), when the Mach number is in the range of 0.6–0.8, a measurement error of ±0.2 °C in T_m (the temperature measured by the FBG) will result in an error in the recovery factor of ±0.02. Therefore, it is possible to observe recovery factor close to 1 during actual measurement.

The variation trends of recovery factor obtained from measurements and simulation calculations are generally consistent, with minor discrepancies attributed to the measurement errors of FBG, assembly errors of probes, as well as nonuniformity and instability of airflow in the wind tunnel.

V. Conclusion

By analyzing the effect of the aerodynamic structure and FBG spectral characteristics on the recovery factor, an optimized design for the aerodynamic structure and grating parameters of the FBG total temperature probe was achieved. The CHT simulation results show that increasing the inner diameter of shield can reduce the influence of low-temperature near-wall airflow on the fiber surface temperature, thereby increasing the recovery factor. Additionally, the closer the location of FBG to the fiber end and the shorter its length, the higher the measured temperature. However, the shorter the FBG length, the lower the temperature measurement accuracy. A 1-mm-long FBG can strike a balance between measured temperature and accuracy. The experimental results show that the large diameter FBG total temperature probe can achieve high recovery factors of 0.92–0.99 in airflow with Mach numbers ranging from 0.3 to 0.8. Especially at low Mach numbers, the recovery factor can be improved by over 21%. This structure has exceeded the level of most traditional thermocouple total temperature probes. Through this optimized design, the technical advantages of the FBG total temperature probe can be fully utilized, providing an efficient and accurate testing means for high-speed airflow total temperature testing.

References

[1] Y. Xiao, Z. Cao, and C. Wang, "The effect of dilution air jets on aero-engine combustor performance," *Int. J. Turbo Jet-Engines*, vol. 36, no. 3, pp. 257–269, Aug. 2019.

[2] M. Tahan, E. Tsoutsanis, M. Muhammad, and Z. A. Abdul Karim, "Performance-based health monitoring, diagnostics and prognostics for condition-based maintenance of gas turbines: A review," *Appl. Energy*, vol. 198, pp. 122–144, Jul. 2017.

[3] E. Fadlun, L. Michelizzi, and M. Laco, "Measurement error influence on gas turbine operability for condition-based maintenance and reliability/availability improvement," Presented at the ASME Turbo Expo, Jun. 2008.

[4] L. Villafañe and G. Paniagua, "Aero-thermal analysis of shielded fine wire thermocouple probes," *Int. J. Thermal Sci.*, vol. 65, pp. 214–223, Mar. 2013.
[5] A. Zeisberger, "Total temperature probes for turbine and combustor applications," Presented at the Int. Symp. Air Breathing Engines, Jan. 2007.
[6] B. Lee, C. Kim, I. Yang, K. Lee, and Y. Lee, "Performance evaluation of a rake used for measuring total pressure and total temperature inside an engine inlet duct," *Int. J. Aeronaut. Space Sci.*, vol. 20, no. 2, pp. 346–354, Jun. 2019.
[7] A. Wolf, A. Dostovalov, K. Bronnikov, M. Skvortsov, S. Wabnitz, and S. Babin, "Advances in femtosecond laser direct writing of fiber Bragg gratings in multicore fibers: Technology, sensor and laser applications," *Opto-Electron. Adv.*, vol. 5, no. 4, pp. 1–21, Apr. 2022.
[8] X. Tian, J. Shi, Y. Wang, Y. She, and L. Li, "Temperature sensor based on fiber Bragg grating combined with a microwave photonic-assisted fiber loop ring down," *Opt. Exp.*, vol. 30, no. 6, pp. 10110–10118, Mar. 2022.
[9] J. A. Flores-Bravo, J. Madrigal, J. Zubia, S. Sales, and J. Villatoro, "Coupled-core fiber Bragg gratings for low-cost sensing," *Sci. Rep.*, vol. 12, no. 1, pp. 1–9, Jan. 2022.
[10] S. Chen, D. Vilchis-Rodriguez, S. Djurovič, M. Barnes, P. Mckeever, and C. Jia, "Direct on chip thermal measurement in IGBT modules using FBG technology—Sensing head interfacing," *IEEE Sensors J.*, vol. 22, no. 2, pp. 1309–1320, Jan. 2022.
[11] L. A. Blanquer et al., "Optical sensors for operando stress monitoring in lithium-based batteries containing solid-state or liquid electrolytes," *Nature Commun.*, vol. 13, no. 1, pp. 1–14, Mar. 2022.
[12] L. Polz, T. Berghaus, M. Klose, A. Zeisberger, H. Bartelt, and J. Roths, "Miniaturized total temperature probe based on fibre Bragg gratings," Presented at the 23rd Int. Conf. Opt. Fiber Sensors (OFS), Jun. 2014.
[13] L. Polz, A. Zeisberger, H. Bartelt, and J. Roths, "Total temperature measurement of fast air streams with fiber-optic Bragg grating sensors," *IEEE Sensors J.*, vol. 16, no. 17, pp. 6596–6603, Sep. 2016.
[14] T. Erdogan, "Fiber grating spectra," *J. Lightw. Technol.*, vol. 15, no. 8, pp. 1277–1294, Aug. 1997.
[15] T. G. Vincent, E. N. Rolfe, K. T. Lowe, and J. A. Schetz, "Aerodynamic analysis of total temperature probe thermal performance using conjugate heat transfer," *J. Thermophys. Heat Transf.*, vol. 33, no. 3, pp. 830–843, Jul. 2019.
[16] R. Gassino, G. Perrone, and A. Vallan, "Temperature monitoring with fiber Bragg grating sensors in nonuniform conditions," *IEEE Trans. Instrum. Meas.*, vol. 69, no. 4, pp. 1336–1343, Apr. 2020.
[17] W. Zhang, X. Lei, Z. Yu, B. Shao, and W. Chen, "Evaluating the effect on demodulation with a comprehensive model of distortions of fiber Bragg grating sensing signals," *J. Lightw. Technol.*, vol. 36, no. 24, pp. 5823–5832, Dec. 15, 2018.

Guoqing Han is currently pursuing the Ph.D. degree in optical engineering with the Key Laboratory of Optoelectronic Technology and Systems Ministry of Education, College of Optoelectronic Engineering, Chongqing University, Chongqing, China.

Jianping Hu received the Ph.D. degree from Northwestern Polytechnical University, Xi'an, China, in 2013.

He is currently an Associate Professor. His main research interests include simulation and experiment about flow and heat transfer involved in aeroengines.

Xianming Liu received the bachelor's degree from Shandong University, Jinan, China, in 2005, and the Ph.D. degree from the Institute of Optics and Electronics, Chinese Academy of Sciences, Beijing China, in 2010.

He is currently an Associate Professor and the Ph.D. Advisor with Chongqing University, Chongqing, China. His main research interests include sensing and testing technology.

Xiaohua Lei, photograph and biography not available at the time of publication.

Peng Zhang, photograph and biography not available at the time of publication.